

Probing and controlling oxygen impurity diffusion in *h*-BN semi-bulk crystals

Cite as: Appl. Phys. Lett. **123**, 252106 (2023); doi: [10.1063/5.0164457](https://doi.org/10.1063/5.0164457)

Submitted: 22 June 2023 · Accepted: 28 November 2023 ·

Published Online: 19 December 2023



View Online



Export Citation



CrossMark

M. Almomhammad, A. Tingsuwatit, Z. Alemoush, J. Li, J. Y. Lin,^{a)} and H. X. Jiang^{a)}

AFFILIATIONS

Department of Electrical and Computer Engineering, Texas Tech University, Lubbock, Texas 79409, USA

^{a)}Authors to whom correspondence should be addressed: hx.jiang@ttu.edu and jingyu.lin@ttu.edu

ABSTRACT

Combining its unique features of ultrawide bandgap (UWBG) and two-dimensional nature, *h*-BN has been explored for emerging applications such as deep ultraviolet optoelectronic devices and single photon emitters. One of the unusual applications of *h*-BN is for solid-state neutron detectors by utilizing the property of high thermal neutron capture cross section of B-10 as well as its UWBG properties. Although a record high detection efficiency of 59% has been attained by *h*-BN detectors, the understanding/minimization of defects and impurities is still needed to further advance the *h*-BN material and detector technologies. We report metal organic chemical vapor deposition growth and oxygen (O) impurity diffusion in thick *h*-BN. The diffusion coefficient (D) of O impurities has been measured via the evolution of an oxygen related emission with the etching depth, providing a value of D of $\sim 2 \times 10^{-13} \text{ cm}^2/\text{s}$ at 1450 °C and supporting the interpretation that oxygen in *h*-BN is a substitutional donor. A multiple-buffer-layer approach was employed to mitigate to a certain degree the issue of oxygen diffusion from sapphire substrate during growth. It was demonstrated that the performance of *h*-BN neutron detectors fabricated from the wafer incorporating multiple buffer layers was significantly improved, as manifested by the enhanced thermal neutron detection efficiency. The advancement of the crystal growth technology of *h*-BN semi-bulk crystals creates applications in optoelectronic and power electronic devices utilizing the UWBG semiconductor properties of *h*-BN, while high efficiency *h*-BN neutron detectors have the potential to supplant the traditional He-3 gas detectors in various application areas by offering the obvious advantages of UWBG semiconductor technologies.

Published under an exclusive license by AIP Publishing. <https://doi.org/10.1063/5.0164457>

Hexagonal boron nitride (*h*-BN) possesses an ultrawide bandgap of about 6 eV and has attracted considerable attention recently for its potential applications in deep UV photonics,^{1–4} 2D materials, and single photon emitters.^{5–8} When enriched with B-10, *h*-BN has demonstrated a great promise for applications for neutron detection due to the unique property of ¹⁰B isotope having a large capture cross section for thermal neutrons ($\sigma = 3840$ barns or $3.84 \times 10^{-21} \text{ cm}^2$).^{9–12} In contrast to existing indirect-conversion solid-state technologies, which rely on coating a thin neutron conversion layer of ⁶Li or ¹⁰B on a bulk semiconductor^{13–15} or formation of micro-structures filled with a ¹⁰B or ⁶Li neutron conversion material,^{16–19} a ¹⁰B containing semiconductor itself performs both functions of neutron conversion and charge carrier generation/collection^{9–12,20,21} and hence potentially affords a theoretical detection efficiency for thermal neutrons approaching 100%.

In ¹⁰B enriched *h*-BN (*h*-¹⁰BN), the density of ¹⁰B atoms is $N(^{10}\text{B}) = 5.5 \times 10^{22}/\text{cm}^3$, which provides an absorption coefficient of $\alpha = N\sigma = 5.5 \times 10^{22} \times 3.84 \times 10^{-21} = 211.2 \text{ cm}^{-1}$, an absorption length of $\lambda = \alpha^{-1} = 47.3 \mu\text{m}$, and an intrinsic efficiency for thermal neutrons of

$$\eta_i(t) = 1 - e^{-t/\lambda}, \quad (1)$$

where t is the detector's layer thickness. Therefore, the theoretical detection efficiency of thermal neutron detectors based on *h*-¹⁰BN approaches 100% for a thickness of $\sim 250 \mu\text{m}$.^{9–12} Equation (1) clearly indicates that realizing high efficiency neutron detectors requires the development of growth processes for wafer scale *h*-BN in large thicknesses. However, *h*-BN bulk crystals produced by the high pressure/high temperature (HP/HT) technique and by the metal flux solution method^{2,22–28} exhibit high material quality, but are very small in crystallite size (1–2 mm), which are impractical for device implementation. Thin film growth processes, such as metal organic vapor deposition (MOCVD), need to be developed for large area semi-bulk *h*-BN wafers (films with large thicknesses) to enable the realization of high efficiency *h*-BN neutron detectors.

In a neutron detector, the measured detection efficiency (η) depends not only on the theoretical efficiency (η_i) described in Eq. (1), but also on the charge collection efficiency (η_c), $\eta = \eta_i \eta_c$.¹⁰ The condition for charge collection and signal detection by a detector is that the

drift length ($E\mu\tau$) of a radiation-generated charge carrier in a field must be greater than its transit length (spacing between the two electrodes, W), i.e.,

$$\frac{W}{E\mu\tau} = \frac{W^2}{V\mu\tau} \ll 1, \quad (2)$$

where V is the applied voltage, E is the applied electric field, and $\mu\tau$ describes the carrier mobility-lifetime product, which is dictated by the overall material quality. This basic charge collection condition implies that the charge collection efficiency is not only determined by the applied electric field (or applied voltage) but also by the overall material quality. While h - ^{10}BN thermal neutron detectors, having a detection area of 1 cm^2 fabricated from a $100\text{ }\mu\text{m}$ thick h - ^{10}BN by combining five lateral detector strips with an average width of 1.3 mm , have attained a record high detection efficiency of 59% at 500 V,¹⁰ further technology advancement requires continuous progress in increasing the wafer thickness and enhancing the overall material quality to improve both the intrinsic efficiency (η_i) and the charge collection efficiency (η_c).

From a practical point of view, it is also highly desirable to increase the detector strip width (W) to enhance the manufacturing yield. However, without a further improvement in the material quality, a wider detector would require a higher applied voltage to support the same charge collection efficiency, based on the understanding provided by Eq. (2). Due to the requirement of a large thickness for providing a high intrinsic detection efficiency according to Eq. (1), a long growth time is needed and therefore, thick h - ^{10}BN materials unavoidably contain oxygen impurities, which were diffused from the sapphire substrate during growth.^{29–31} Previous studies have provided strong evidence that the presence of oxygen impurities impacted the performance of h -BN neutron detectors.^{10,29–31} However, the effects of oxygen in h -BN are not yet fully understood. Theoretical studies suggested that oxygen can be incorporated into h -BN as a substitutional donor by occupying N site (O_N), which concomitantly can lead to the incorporation of boron vacancy (V_B)-hydrogen complex ($\text{V}_\text{B}-\text{H}/\text{V}_\text{B}-2\text{H}$) and O interstitial (O_i) deep level acceptors because their formation energies tend to decrease with the Fermi level shifting toward the conduction band edge in the presence of O_N .³² It is expected that these electron-compensating deep level acceptors can capture and scatter neutron-generated charge carriers and are detrimental to the charge collection efficiency of h -BN thermal neutron detectors. As such, finding effective strategies to mitigate the impact of oxygen diffusion is also highly desired.

In this work, h - ^{10}BN semi-bulk wafers ($\sim 100\text{ }\mu\text{m}$ in thickness) were produced by MOCVD and studied by photoluminescence (PL) emission spectroscopy and secondary-ion mass spectrometry (SIMS), with the aim to obtain an improved understanding of the nature of oxygen impurities in h -BN. The observed impurity related PL emission peak position near 3.8 eV together with a previous theoretical understanding³² suggested that this emission can be attributed to a donor-acceptor pair (DAP) transition involving O_N donor and $\text{V}_\text{B}-\text{H}/\text{V}_\text{B}-2\text{H}$ acceptors. PL emission intensity in conjunction with a dry etching technique³³ allows the probing of the relative impurity concentration distribution with respect to the h -BN/sapphire interface, which resembles the oxygen impurity profile probed by SIMS. From these measurements, the oxygen diffusion coefficient was deduced, and the results further backing the interpretation that oxygen impurities involved in the PL emission are substitutional rather than interstitial type.

Adopting a multiple-buffer-layer strategy allowed the realization of a lateral strip thermal neutron detector with an increased width and improved performance over our previous attainment, potentially paving the way for achieving high efficiency and high sensitivity thermal neutron detectors while enhancing the manufacturing yield by simplifying the device fabrication processes.

Semi-bulk wafers of h - ^{10}BN were synthesized by MOCVD on the sapphire substrate at a growth temperature of $1450\text{ }^\circ\text{C}$.^{9–12,29–31} Trimethylboron (TMB) with a vendor specified ^{10}B isotope enrichment of 99.9% and ammonia (NH_3) were used as the precursors for the growth of h - ^{10}BN . Hydrogen was utilized as a carrier gas. As shown schematically in Fig. 1(a), freestanding h - ^{10}BN wafer was then obtained via self-separation during cooling down after MOCVD growth, due to h -BN's layered structure and thermal expansion coefficient that is different from that of sapphire. The freestanding wafer was then cut into desired shape by laser dicing for characterization and device fabrication. Figure 1(b) is a micrograph of a freestanding h - ^{10}BN sample used for PL study. For the PL measurements, a pulsed excimer laser emitting at 193 nm was used as an excitation source, which exceeds the bandgap of h -BN, and the PL emission spectra were collected using an optical fiber coupled with a spectrometer (Ocean Optics USB2000+). A SF_6 chemistry based inductively coupled plasma (ICP) dry etching technique³³ was employed to remove successively the surface, which was in contact with sapphire after self-separation for the purpose of probing the PL spectra at different depths from the sapphire/ h -BN interface. We expect that ICP dry etch may introduce surface damage, but the concentration of oxygen impurities on the h -BN surface should not be affected since no oxygen was used during ICP etching and ICP etching conditions were kept the same.

Figure 2(a) plots the room temperature PL spectra measured for a freestanding sample prior to ICP dry etching (non-etched) and at different depths from the surface (h -BN/sapphire/interface). The PL emission spectra plotted in Fig. 2(a) were normalized to the broad emission peak near 3.8 eV of the non-etched sample and revealed that the emission intensity near 3.8 eV decreases with the etching depth. To reveal the physical origin of the main PL emission line, we present in Fig. 2(b) a band edge energy diagram of h -BN,³¹ showing an energy bandgap value of $\sim 6.0\text{ eV}$ with the conduction band minimum (CBM)

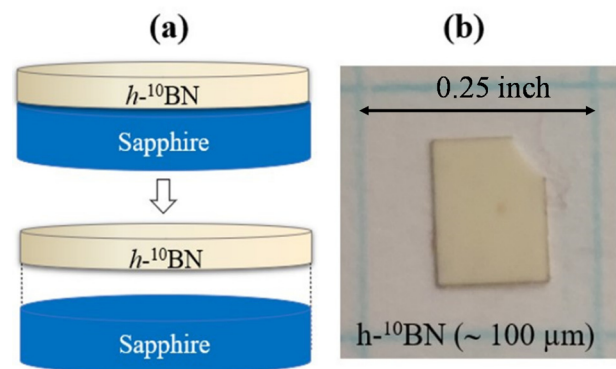


FIG. 1. (a) Schematic of h - ^{10}BN thick layers grown on sapphire and realization of freestanding h - ^{10}BN wafer via self-separation during cooling down after MOCVD growth. (b) Micrograph of a $100\text{ }\mu\text{m}$ thick freestanding h - ^{10}BN sample used for photoluminescence (PL) measurements.

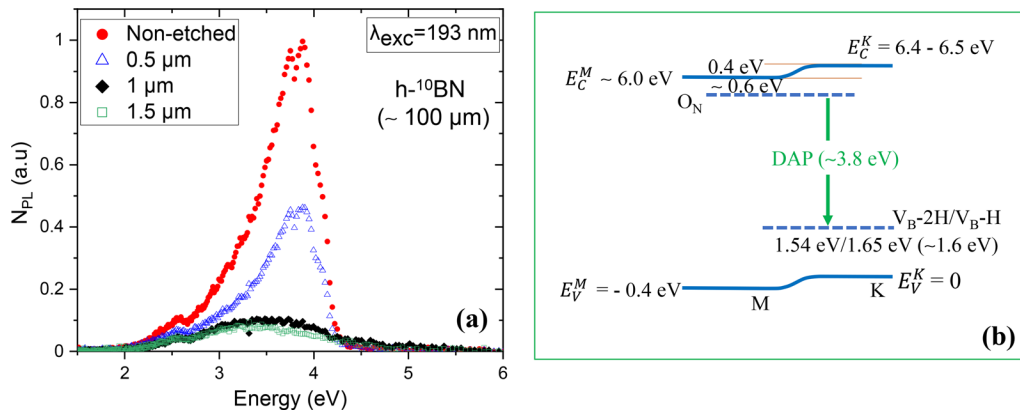


FIG. 2. (a) Room temperature photoluminescence (PL) spectra under excitation by an excimer laser at 193 nm of a freestanding 100 μm thick $h^{-10}BN$ wafer, measured at different depths from the h -BN/sapphire interface. The depth was controlled by removing successively by ICP dry etching the surface, which was in contact with sapphire substrate during growth. (b) Band edge energy diagram of h -BN, revealing the physical origin of the PL emission lines near 3.8 eV. The energy diagram also reflects the nature of indirect energy bandgap with the conduction band minimum (CBM) and the valence band maximum (VBM) located at M- and K-point, respectively, as well as the effect of a minimum direct bandgap in h -BN. [Adapted with permission from Grenadier *et al.*, Appl. Phys. Express **15**, 051005 (2022). Copyright 2022 IOP Publishing; Fig. 3(b) of Ref. 31.]

located around M-point and valence band maximum (VBM) located around K-point in the Brillouin zone.^{34,35} The measured/predicted O_N donor level is at about 0.56 eV/0.61 eV (~ 0.6 eV) below the CBM,^{29,32} and the predicted V_{B-H}/V_{B-2H} acceptor level is at 1.65 eV/1.54 eV above the VBM.³² The band diagram, thus, suggests that the observed impurity emission peak near 3.8 eV is due to a donor-acceptor pair (DAP) recombination involving O_N donors and V_{B-H}/V_{B-2H} acceptors, as indicated by the bold green arrow line in Fig. 2(b). A more careful inspection reveals that the dominant emission near 3.8 eV consists of two emission lines separated by ~ 0.1 eV, which can be attributed to DAP recombination corresponding to $O_N \rightarrow V_{B-H}$ and $O_N \rightarrow V_{B-2H}$ transitions, respectively.

With the origin of the emission lines near 3.8 eV being identified, the relative O impurity concentration can be measured by probing the PL emission intensity near 3.8 eV as a function of the etching depth from the h -BN/sapphire interface. Figure 3(a) plots the integrated PL emission intensity vs the etching depth. Indeed, a systematic decrease in the integrated PL emission intensity at 3.8 eV was found, which

further confirms that O impurities were diffused from the sapphire substrate. To support this interpretation, SIMS measurements were performed to probe the profile of oxygen concentration as a function of the depth measured from the surface originally in contacting with sapphire and the results are shown in Fig. 3(b), which revealed a trend that is exactly like the reduction observed in the normalized PL intensity shown in Fig. 3(a). More specifically, within the initial 1 μm of etching depth, the oxygen concentration decreased from 1.26×10^{20} to 1.89×10^{19} atoms/cm³ (nearly one order of magnitude reduction), whereas the PL emission intensity decreased from 1 to 0.1. This clear correlation between the PL and SIMS measurement results further confirm that the emission lines near 3.8 eV are related to the diffusion of O impurities from the sapphire substrate.

It is also worth noting that the observed PL peak position shown in Fig. 2(a) exhibits a redshift with the etching depth, which in turn further supports our interpretation that the main PL emission line is of a DAP in nature involving O_N donors. It is well known that the peak position of a DAP recombination follows the relation of $h\nu$ (r)

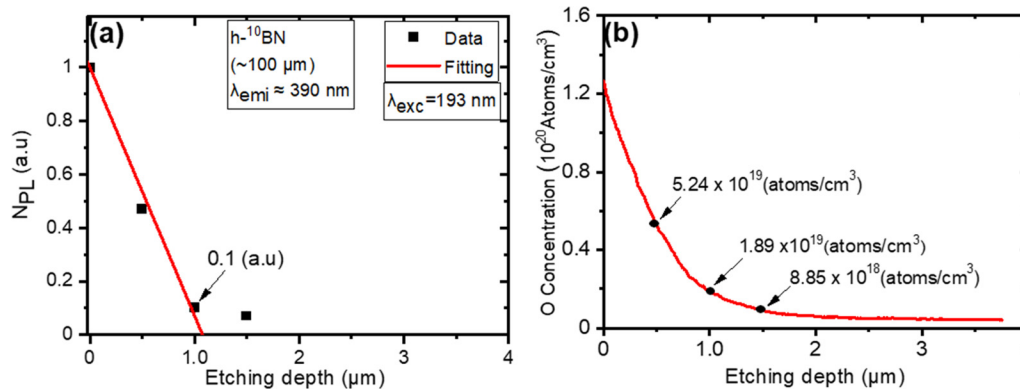


FIG. 3. (a) Plot of the integrated intensity of the PL emission line measured in Fig. 2(a) as a function of the etching depth. The red curve is a fitting using Eq. (4). (b) Oxygen concentration profile in a freestanding $h^{-10}BN$ wafer probed by SIMS measurements. The concentrations were measured from the surface originally in contact with sapphire.

$= E_g - (E_D + E_A) + \frac{e^2}{\epsilon r}$, where E_D and E_A are the donor and acceptor ionization energies, respectively, r is the mean donor-acceptor (D-A) separation distance, and ϵ is the dielectric constant.³⁶ SIMS measurement results shown in Fig. 3(b) indicate that the oxygen donor concentration decreases, and hence, the mean D-A separation distance (r) increases with the etching depth. Therefore, the observed PL peak position is expected to exhibit a redshift with increasing the etching depth.

Based on the analysis of the PL emission origin, the systematic decrease in the PL emission intensity with the etching depth can then be understood in terms of the O impurity concentration decreasing with the depth following the diffusion process. For simplicity, assuming an infinite oxygen source from the sapphire substrate during growth, the depth profile of the oxygen concentration can be described by Fick's second law, $n(d, t) = n_o \operatorname{erfc}(\frac{d}{2\sqrt{Dt}})$, where d is the depth measured from the surface originally in contacting with sapphire, erfc is the complementary error function, D is the diffusion coefficient of oxygen impurities in h -BN, and t denotes the total growth time. The complementary error function is $\operatorname{erfc}(z) = 1 - \operatorname{erf} z$, with $z = (\frac{d}{2\sqrt{Dt}})$ and $\operatorname{erf} z$ being the Gauss error function, which can be written as $\operatorname{erf} z = \frac{2}{\sqrt{\pi}} \int_0^z e^{-x^2} dx$. As an approximation of the error function, the initial two terms of the Taylor series will be used, which gives

$$n(d, t) = n_o \left[1 - 2 \left(\frac{d}{2\sqrt{Dt}\pi} \right) \right], \quad (3)$$

and therefore, the normalized PL emission intensity as a function of etching depth (d) also takes the form of Eq. (3) as

$$N_{PL} = N_o \left[1 - 2 \left(\frac{d}{2\sqrt{Dt}\pi} \right) \right]. \quad (4)$$

Fitting experimental data in Fig. 3(a) with Eq. (4) yields a value of $D = 2.1 \times 10^{-13} \text{ cm}^2/\text{s}$ at 1450°C . It is worth to point out that the trends of both the experimentally observed etching depth dependencies of PL intensity and O concentration probed by SIMS shown in Figs. 3(a) and 3(b) follow exactly the trend of the diffusion process described by Fick's second law. However, we used an approximation and kept only the initial two terms of the Taylor series for the error function to reduce the diffusion process to a linear relationship of Eqs. (3) and (4) for simplicity. Because we are using a linear fit and the PL

intensity hardly changes with the etching depth beyond $1 \mu\text{m}$, we, thus, included only PL data from the first $1 \mu\text{m}$ after etching in the linear fit to obtain the diffusion coefficient (D). Although the value of D obtained from the linear fit in Fig. 3(a) is an approximation, it should provide a reasonable first order estimation.

It is important to note that the measured oxygen impurity diffusion constant in h -BN is on the same order as those of substitutional impurities in Si (on the order of 10^{-15} – $10^{-13} \text{ cm}^2/\text{s}$ at 1300°C) but is about eight orders of magnitude lower than the diffusion constants of interstitial impurities in Si (on the order of 10^{-6} – $10^{-5} \text{ cm}^2/\text{s}$).³⁷ Moreover, the measured diffusion coefficient of O in h -BN is also very close to (about 4 times larger than) those of Si and O substitutional impurities in AlN of about $5 \times 10^{-14} \text{ cm}^2/\text{s}$ at 1450°C .³⁸ These results together further suggest that the emission line near 3.8 eV in thick h -BN is related to substitutional oxygen impurities, namely, O_N .

Prior and recent developments in III-nitride materials and devices have demonstrated that low temperature multiple-buffer-layers grown using a gradual increase in the growth temperatures serve as an effective dislocation filter and improve the performance of top active layers.^{39–41} We adopted this multiple-buffer-layer approach with the aim to reduce the impact of oxygen diffusion on the performance of thermal neutron detectors. For a comparison study, in "sample 1," a single BN buffer layer of about 20 nm in thickness was deposited at about 800°C prior to the deposition of the top thick h - ^{10}BN , as illustrated in the inset of Fig. 4(a), while "sample 2" consists of three buffer layers each of 20 nm in thickness deposited at a higher temperature than the previous layer of 800 , 1000 , and 1200°C , respectively, as illustrated the inset of Fig. 4(b).

To directly evaluate the effectiveness of this multiple-buffer-layer approach in the growth of h -BN thick wafers, thermal neutron detector strips of 1.7 mm in width in a lateral geometry were fabricated from sample 1 and sample 2, as depicted in the insets of Figs. 4(a) and 4(b). Metal contacts consisting of a bi-layer of Ni (100 nm)/Au (40 nm) were deposited on the two edges of the h - ^{10}BN strips using e-beam evaporation via a mask and wire bonding was performed to create an electrical connection between the deposited metal contacts and the bonding pads of a semiconductor device package. The reason for utilizing a lateral strip detector geometry has been extensively

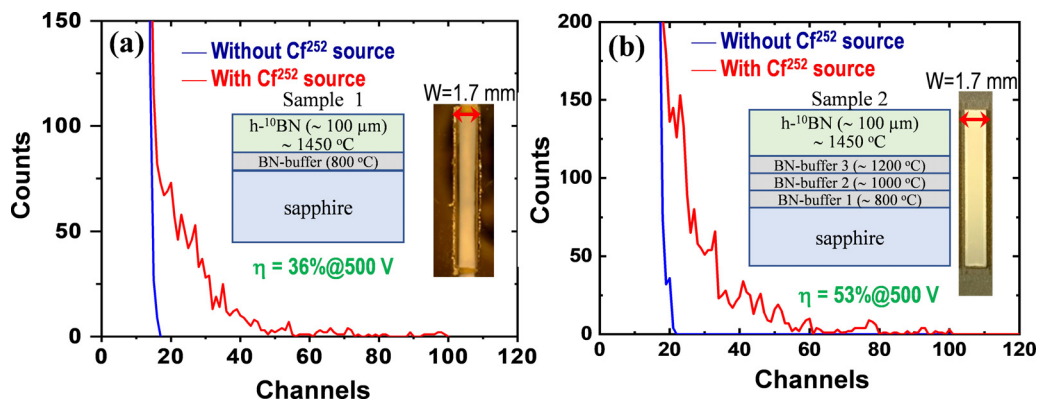


FIG. 4. Pulse height spectra of h - ^{10}BN lateral detector strips of 1.7 mm in width fabricated from (a) sample 1 and (b) sample 2. Red curves are the responses to thermal neutrons at 500 V , and the blue curves are the background (or dark) counts measured at the same bias voltage (500 V). The schematic layer structures of samples and optical images of the finished devices are shown in the insets.

discussed previously,^{9–12,30} which include taking the advantages of the outstanding lateral transport properties of *h*-BN, a reduced surface recombination field, and a reduced device capacitance in support of an enhanced charge collection efficiency under a moderate bias voltage compared to a vertical planar detector of the same detection area.⁹ Moreover, because the carrier transport occurs in the lateral direction (in the *c*-plane), the interfaces between the very thin multiple buffer layers are expected to have a negligible effect on the charge collection efficiencies of these thick lateral detectors.

To measure the thermal neutron detection efficiency, a depleted sealed neutron source of californium-252 (²⁵²Cf) from (Frontier technologies) was employed as a neutron source. A high-density polyethylene (HDPE) moderator was constructed for the storage of the ²⁵²Cf source and moderating the fast neutrons to thermal neutrons, as shown in Fig. 5.⁴² When the ²⁵²Cf source is placed at location (A), most neutrons are stopped by HDPE. When the ²⁵²Cf source is placed at location (B), most neutrons released from the front surface of the HDPE moderator are thermal neutrons, characterized by their kinetic energy ranging between 1 and 100 meV, with a peak energy at 25 meV. The detection electronics consist of a charge sensitive preamplifier, pulse shaping amplifier, and multi-channel analyzer.^{9,10} The shielded detectors were placed 30 cm away from the front surface of the HDPE moderator.

Figures 4(a) and 4(b) plot the measured pulse height spectra of the two *h*-¹⁰B detectors fabricated from (a) sample 1 and (b) sample 2, respectively. For each detector, the dark spectrum (blue curve) was recorded in the absence of any radiation, while the spectrum (red) under thermal neutron irradiation was measured at the same bias voltage. Previous results have demonstrated that *h*-¹⁰B detectors have a negligible response to gamma photons because ¹⁰B and N are low atomic number elements.^{9,10} The pulse height spectrum under thermal neutron radiation was integrated beyond the highest dark channel (low level discriminator) to obtain the total number of counts. By comparing the total number of counts detected by the *h*-¹⁰B detector to

that of a commercial ⁶LiF filled 4 cm² micro-structured semiconductor neutron detector (MSND Domino™ V4) formed by combining four 1 cm² detectors with a certified detection efficiency of 30%, the detection efficiencies (η) of our *h*-¹⁰B detectors were determined. The measured detection efficiencies of the detectors fabricated from sample 1 and sample 2 are 36% and 53% at 500 V, respectively. We would like to point out that detectors have been fabricated from *h*-¹⁰B wafers grown under identical conditions without any buffer layer(s), the measured thermal detection efficiency for the same thickness is \sim 25% at 500 V. The results shown in Fig. 4 suggest that the multiple-buffer-layer approach is effective in reducing the impact of oxygen impurity diffusion and improving the charge collection efficiency and hence the thermal neutron detection efficiency. In terms of the detection efficiency per applied electric field, the 53% detection efficiency measured from the 1.7 mm wide detector fabricated from sample 2 in fact has outperformed the previous reported best efficiency of 59% for detector strips of 1.3 mm wide at the same applied voltage of 500 V.¹⁰ The promising results shown in Fig. 4 also call for more detailed comparison studies in crystalline qualities, carrier mobilities, microstructures, and impurity diffusion coefficients for materials produced with and without the use of the multiple-buffer-layer approach to clarify whether the effects are more related to the buffer layer thickness or the conditions of buffer layer growth.

In summary, the diffusion of oxygen impurities in *h*-¹⁰B and impact of oxygen impurities on the performance of *h*-¹⁰B thermal neutron detectors have been investigated. The diffusion coefficient (*D*) of oxygen impurities in *h*-BN was measured via probing an oxygen related PL emission line as a function of the etching depth in a free-standing *h*-BN wafer after self-separation from a sapphire substrate. The results revealed a value of *D* of about 2×10^{-13} cm²/s at 1450 °C, supporting the understanding that oxygen impurities in thick *h*-BN are substitutional donors. The measured *D* value is about four times larger than those of Si and O substitutional impurities in AlN. Thermal neutron detectors fabricated from *h*-¹⁰B grown with a multiple-buffer-layer approach outperformed those fabricated from wafers with no buffer or with a single buffer layer, which suggests that such an approach is useful in mitigating the issue of oxygen diffusion in the growth of thick *h*-BN wafers on a sapphire substrate. As a benchmark (or a baseline), the dominant PL emission lines in high-quality *h*-BN millimeter-sized bulk crystals produced by a high pressure/temperature technique are due to the band edge transitions near 215 nm (\sim 5.77 eV).²² Therefore, our goal is to produce *h*-BN large wafers exhibiting predominantly the band edge transitions by monitoring/eliminating impurity/defect related PL emission lines. The development of *h*-BN semi-bulk crystals with improved quality is expected to create opportunities in UWBG semiconductor optoelectronic and power electronics, while high efficiency neutron detectors based UWBG *h*-BN semiconductor will create unprecedented applications in nuclear energy, national security, medical/health care, and material sciences.

This research is supported by DOE ARPA-E (No. DE-AR0001552, monitored by Dr. Olga Spahn, Dr. Isik Kizilyalli, and Dr. Eric Carlson). Jiang and Lin are grateful to the AT&T Foundation for the support of Ed Whitacre and Linda Whitacre endowed chairs. The data that support the findings of this study are available within this manuscript.

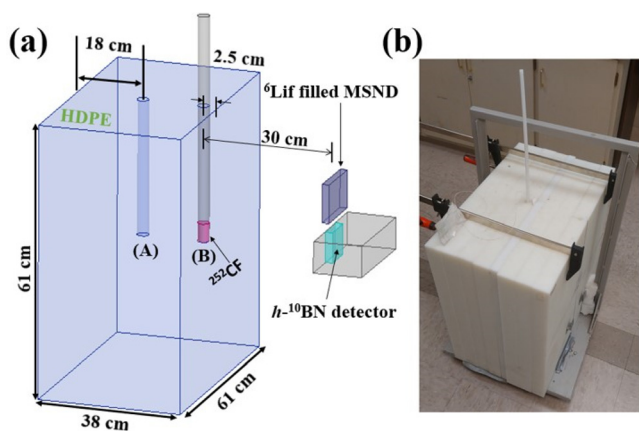


FIG. 5. (a) Schematic of thermal neutron source used in this work, which consists of a ²⁵²Cf source moderated by a high-density polyethylene (HDPE) block. Adopted with permission from Doan *et al.*, Nucl. Instrum. Methods Phys. Res., Sect. A **783**, 121 (2015). Copyright 2015 Elsevier; Fig. 3(b) of Ref. 42. The thermal neutron detection efficiencies of *h*-¹⁰B detectors were calibrated by placing the detectors at 30 cm from the HDPE cube front face and side-by-side with a ⁶LiF filled micro-structured semiconductor neutron detector (MSND). (b) Photograph of the actual thermal neutron source setup.

AUTHOR DECLARATIONS

Conflict of Interest

The authors have no conflicts to disclose.

Author Contributions

Musab Abdallah Almomhammad: Data curation (equal); Formal analysis (equal); Investigation (equal); Methodology (equal); Validation (equal); Visualization (equal); Writing – original draft (equal). **Attasit Tingsuwatit:** Data curation (equal); Formal analysis (equal); Investigation (equal); Methodology (equal); Validation (equal); Visualization (equal). **Zaid Alemoush:** Data curation (equal); Formal analysis (equal); Investigation (equal); Methodology (equal); Validation (equal); Visualization (equal). **Jing Li:** Data curation (equal); Formal analysis (equal); Investigation (equal); Methodology (equal); Software (equal); Supervision (equal); Validation (equal); Visualization (equal). **Jingyu Lin:** Conceptualization (equal); Data curation (equal); Formal analysis (equal); Funding acquisition (equal); Investigation (equal); Methodology (equal); Project administration (equal); Resources (equal); Supervision (equal); Validation (equal); Visualization (equal); Writing – original draft (equal); Writing – review & editing (equal). **Hongxing Jiang:** Conceptualization (equal); Data curation (equal); Formal analysis (equal); Funding acquisition (equal); Investigation (equal); Methodology (equal); Project administration (equal); Resources (equal); Supervision (equal); Validation (equal); Visualization (equal); Writing – original draft (equal); Writing – review & editing (equal).

DATA AVAILABILITY

The data that support the findings of this study are available within the article.

REFERENCES

- ¹Y. Kubota, K. Watanabe, O. Tsuda, and T. Taniguchi, *Science* **317**, 932 (2007).
- ²K. Watanabe, T. Taniguchi, T. Niiyama, K. Miya, and M. Taniguchi, *Nat. Photonics* **3**, 591 (2009).
- ³S. Majety, J. Li, X. K. Cao, R. Dahal, B. N. Pantha, J. Y. Lin, and H. X. Jiang, *Appl. Phys. Lett.* **100**, 061121 (2012).
- ⁴H. X. Jiang and J. Y. Lin, “Hexagonal boron nitride for deep ultraviolet photonic devices” (in special section “Deep UV LEDs,” Guest editors: Jung Han, Hiroshi Amano and Leo Scholwalter), *Semicond. Sci. Technol.* **29**, 084003 (2014).
- ⁵T. T. Tran, C. Elbadawi, D. Totonjian, C. J. Lobo, G. Grosso, H. Moon, D. R. Englund, M. J. Ford, I. Aharonovich, and M. Toth, *ACS Nano* **10**, 7331 (2016).
- ⁶N. R. Jungwirth, B. Calderon, Y. Ji, M. G. Spencer, M. E. Flatté, and G. D. Fuchs, *Nano Lett.* **16**, 6052 (2016).
- ⁷Z. Shotan, H. Jayakumar, C. R. Consideine, M. Mackoito, H. Fedder, J. Wrachtrup, A. Alkauskas, M. W. Doherty, V. M. Menon, and C. A. Meriles, *ACS Photonics* **3**, 2490 (2016).
- ⁸Y. Wang, J. Lee, J. Berezovsky, and P. X. L. Feng, *Appl. Phys. Lett.* **118**, 244003 (2021).
- ⁹A. Maity, T. C. Doan, J. Li, J. Y. Lin, and H. X. Jiang, *ibid.* **109**, 072101 (2016); **111**, 033507 (2017); **114**, 222102 (2019).
- ¹⁰A. Maity, S. J. Grenadier, J. Li, J. Y. Lin, and H. X. Jiang, *Appl. Phys. Lett.* **116**, 142102 (2020).
- ¹¹J. Li, A. Maity, S. J. Grenadier, J. Y. Lin, and H. X. Jiang, *Appl. Phys. Lett.* **118**, 092102 (2021).
- ¹²A. Tingsuwatit, A. Maity, S. J. Grenadier, J. Li, J. Y. Lin, and H. X. Jiang, *Appl. Phys. Lett.* **120**, 232103 (2022).
- ¹³A. Rose, *Nucl. Instrum. Methods* **52**, 166 (1967).
- ¹⁴D. S. McGregor, R. T. Klann, H. K. Gersch, and Y. H. Yang, *Nucl. Instrum. Methods Phys. Res., Sect. A* **466**, 126 (2001).
- ¹⁵S. Adenwalla, P. Welsch, A. Harken, J. I. Brand, A. Sezer, and B. W. Robertson, *Appl. Phys. Lett.* **79**, 4357 (2001).
- ¹⁶R. J. Nikolic, A. M. Conway, C. E. Reinhardt, R. T. Graff, T. F. Wang, N. Deo, and C. L. Cheung, *Appl. Phys. Lett.* **93**, 133502 (2008).
- ¹⁷R. J. Nikolic, C. L. Cheung, C. E. Reinhardt, and T. F. Wang, *Proc. SPIE* **6013**, 601305 (2005).
- ¹⁸A. M. Conway, T. F. Wang, N. Deo, C. L. Cheung, and R. J. Nikolic, *IEEE Trans. Nucl. Sci.* **56**, 2802 (2009).
- ¹⁹R. Dahal, K. C. Huang, J. Clinton, N. LiCausi, J.-Q. Lu, Y. Danon, and I. Bhat, *Appl. Phys. Lett.* **100**, 243507 (2012).
- ²⁰K. P. Ananthanarayanan, P. J. Gielisse, and A. Choudry, *Nucl. Instrum. Methods* **118**, 45 (1974).
- ²¹K. Osberg, N. Schemm, S. Balkir, J. I. Brand, M. S. Hallbeck, P. A. Dowben, and M. W. Hoffman, *IEEE Sens. J.* **6**, 1531 (2006).
- ²²K. Watanabe, T. Taniguchi, and H. Kanda, *Nat. Mater.* **3**, 404 (2004).
- ²³T. Ishii and T. Sato, *J. Cryst. Growth* **61**, 689 (1983).
- ²⁴T. Taniguchi and K. Watanabe, *J. Cryst. Growth* **303**, 525 (2007).
- ²⁵N. D. Zhigadlo, *J. Cryst. Growth* **402**, 308 (2014).
- ²⁶J. Li, J. Wang, X. Zhang, C. Elias, G. Ye, D. Evans, G. Eda, J. M. Redwing, G. Cassabois, B. Gil, P. Valvin, R. He, B. Liu, and J. H. Edgar, *Chem. Mater.* **32**, 5066 (2020).
- ²⁷J. Li, X. K. Cao, T. B. Hoffman, J. H. Edgar, J. Y. Lin, and H. X. Jiang, *Appl. Phys. Lett.* **108**, 122101 (2016).
- ²⁸R. V. Gorbachev, I. Riaz, R. R. Nair, R. Jalil, L. Britnell, B. D. Belle, E. W. Hill, K. S. Novoselov, K. Watanabe, T. Taniguchi, A. K. Geim, and P. Blake, *Small* **7**, 465 (2011).
- ²⁹S. J. Grenadier, A. Maity, J. Li, J. Y. Lin, and H. X. Jiang, *Appl. Phys. Lett.* **112**, 162103 (2018).
- ³⁰S. J. Grenadier, A. Maity, J. Li, J. Y. Lin, and H. X. Jiang, “Electrical transport properties of hexagonal boron nitride epilayers,” *Ultrawide Bandgap Semiconductors*, edited by Y. Zhao (Elsevier, Amsterdam, 2021), Vol 107, Chap. 12.
- ³¹S. J. Grenadier, A. Maity, J. Li, J. Y. Lin, and H. X. Jiang, *Appl. Phys. Express* **15**, 051005 (2022).
- ³²L. Weston, D. Wickramaratne, M. Mackoito, A. Alkauskas, and C. G. Van de Walle, *Phys. Rev. B* **97**, 214104 (2018).
- ³³S. Grenadier, J. Li, J. Y. Lin, and H. X. Jiang, *J. Vac. Sci. Technol., A* **31**, 061517 (2013).
- ³⁴B. Arnaud, S. Lebègue, P. Rabiller, and M. Alouani, *Phys. Rev. Lett.* **96**, 026402 (2006).
- ³⁵L. Artús, M. Feneberg, C. Attacalite, J. H. Edgar, J. Li, R. Goldhahn, and R. Cuscó, *Adv. Photonics Res.* **2**, 2000101 (2021).
- ³⁶J. I. Pankove, *Optical Processes in Semiconductors (Dover Books on Physics)*, 2nd ed. (Dover Publications, Inc. New York, 2010).
- ³⁷S. W. Jones, see http://www-eng.lbl.gov/~shuman/NEXT/MATERIALS&COMPONENTS/Xe_damage/Diffusionin%20siliconpdf.pdf for “Diffusion in Silicon.”
- ³⁸H. Okumura, Y. Watanabe, T. Shibata, K. Yoshizawa, A. Uedono, H. Tokunaga, S. Koseki, T. Arimura, S. Suihkonen, and T. Palacios, *Jpn. J. Appl. Phys., Part 1* **61**, 026501 (2022).
- ³⁹T. M. Al tahtamouni, J. Y. Lin, and H. X. Jiang, *J. Appl. Phys.* **113**, 123501 (2013).
- ⁴⁰P. Chan, S. P. DenBaars, and S. Nakamura, *Appl. Phys. Lett.* **119**, 131106 (2021).
- ⁴¹X. Yang, S. Nitta, M. Pristovsek, Y. Liu, Y. Liao, M. Kushimoto, Y. Honda, and H. Amano, *2D Mater.* **7**, 015004 (2019).
- ⁴²T. C. Doan, S. Majety, S. Grenadier, J. Li, J. Y. Lin, and H. X. Jiang, *Nucl. Instrum. Methods Phys. Res., Sect. A* **783**, 121 (2015).